MONTANA STATE UNIVERSITY

Measuring surface temperature of isolated neutron stars and related problems
by Marcus Alton Teter

A dissertation submitted in partial fulfillment of the requirements for the degree of Doctor of Philosophy in Physics
Montana State University

Abstract:
New and exciting results for measuring neutron star surface temperatures began with the successful launch of the Chandra X-ray observatory. Among these results are new detections of neutron star surface temperatures which have made it possible to seriously test neutron star thermal evolution theories. The important new temperature determination of the Vela pulsar (Pavlov, et al., 2001a) requires a non-standard cooling scenario to explain it.

Apart from this result, we have measured PSR B1055-52's surface temperature in this thesis, determining that it can be explained by standard cooling with heating. Our spectral fit of the combined data from ROSAT and Chandra have shown that a three component model, two thermal blackbodies and an non-thermal power-law, is required to explain the data. Furthermore, our phase resolved spectroscopy has begun to shed light on the geometry of the hot spot on PSR B1055-52's surface as well as the structure of the magnetospheric radiation. Also, there is strong evidence for a thermal distribution over its surface. Most importantly, the fact that PSR B1055-52 does not have a hydrogen atmosphere has been firmly established.

To reconcile these two key observations, on the Vela pulsar and PSR B1055-52, we tested neutron star cooling with neutrino processes including the Cooper pair neutrino emission process. Overall, it has been found that a phase change associated with pions being present in the cores of more massive neutron stars explains all current of the data. A transition from neutron matter to pion condensates in the central stellar core explains the difference between standard and non-standard cooling scenarios, because the superfluid suppression of pion cooling will reduce the emissivity of the pion direct URCA process substantially. A neutron star with a mass of 1.2M with a medium stiffness equation of state and a T72 type neutron superfluid models the standard cooling case well. A neutron star of 1.4M, with a pion core, with the same type of equation of state modified for pion matter and a modified El-0.6 pion superfluid model is the best option for the non-standard case. The results also suggest that the equation of state for neutron stars may have to be stiffer than medium.

Furthermore, our observational results from two other sources, SGR 1900+14 and 1E1207.4-5209, have helped us to expand the understanding of isolated neutron stars. The Chandra observation of SGR 1900+14 has strengthened the case that it is a magnetar, as the pulsed fraction and the spectral fits suggest a blackbody plus power-law model is prefered. Also, our analysis of the Chandra data of 1E1207.4-5209 suggests that it should have a hydrogen atmosphere. Future observations will certainly give even better insight to both of these objects, as well as PSR B1055-52.

MEASURING SURFACE TEMPERATURE OF ISOLATED NEUTRON STARS AND RELATED PROBLEMS.

by

Marcus Alton Teter

A dissertation submitted in partial fulfillment
of the requirements for the degree

of

Doctor of Philosophy

in

Physics

MONTANA STATE UNIVERSITY — BOZEMAN
Bozeman, Montana

December 2001

APPROVAL

of a dissertation submitted by

Marcus Alton Teter

This dissertation has been read by each member of the dissertation committee, and has been found to be satisfactory regarding content, English usage, format, citations, bibliographic style and consistency, and is ready for submission to the College of Graduate Studies.

Sachiko Tsuruta, Ph. D. _____ 12/3/2001
(Signature) Date

Approved for the Department of Physics

John C. Hermanson, Ph. D. _____ 12-3-01
(Signature) Date

Approved for the College of Graduate Studies

Bruce R. McLeod, Ph. D. _____ 12-10-01
(Signature) Date

STATEMENT OF PERMISSION TO USE

In presenting this dissertation in partial fulfillment of the requirements for a doctoral degree at Montana State University — Bozeman, I agree that the Library shall make it available to borrowers under rules of the Library. I further agree that copying of this thesis is allowable only for scholarly purposes, consistent with "fair use" as prescribed in the U. S. Copyright Law. Requests for extensive copying or reproduction of this thesis should be referred to University Microfilms International, 300 North Zeeb Road, Ann Arbor, Michigan, 48106, to whom I have granted "the exclusive right to reproduce and distribute my dissertation in and from microform along with the non-exclusive right to reproduce and distribute my abstract in any format in whole or in part."

Signature M. a. Peterson

Date 3 DEC 2001

ACKNOWLEDGEMENTS

I would like to thank Dr. G. Pavlov at The Pennsylvania State University department of Astronomy for his advise on the *Chandra* data analysis.

This research was sponsored in part by SAO grants GO0-1131A and GO0-1012X.

TABLE OF CONTENTS

1 INTRODUCTION 1

2 *CHANDRA* X-RAY OBSERVATORY 12
Introduction 12
Data Reduction 14

3 *CHANDRA* OBSERVATION OF PSR B1055-52 20
Introduction 20
Previous Observations and Results 20
Our *Chandra* Observation and Data Reduction 24
Our Results 26
One-Dimensional Spatial Results 26
Timing Results 28
Phase Integrated Spectral Analysis 31
Phase Resolved Spectroscopy 41
Discussion 45

4 *CHANDRA* OBSERVATIONS OF SGR 1900+14 51
Introduction 51
Magnetars 51
Soft Gamma-ray Repeaters(SGR) 52
Previous Outbursts of SGR 1900+14 53
April 2001 Event 54
Our Results 55
Our Timing Results 56
Our Phase Integrated Spectral Analysis 63

Our Phase Resolved Spectral Analysis 66
Discussion 68

5 *CHANDRA* OBSERVATIONS OF 1E1207.4-5209 72
Introduction 72
Earlier Observations and Results 73
Chandra Observation and Previous Results 73
Our New Results from the *Chandra* Observation 74
Results of Our Timing Analysis 75
Results of Our Phase Integrated Spectral Analysis 75
Results of Our Phase Resolved Spectral Analysis 78
Discussion 79

6 FUTURE OBSERVATIONS 83
Future Missions 83
Future Observations of Neutron Stars 83

7 COOPER PAIR NEUTRINO EMISSIVITY AND COOLING OF NEUTRON STARS 86
Introduction 86
Theoretical Background 87
Standard Neutrino Emission Mechanisms 89
Non-standard Neutrino Emission Mechanisms 90
Cooper Pair Neutrino Emission Mechanisms 92
Superfluid Models 97
Effects Upon Standard Cooling 99
Effects Upon Non-Standard Cooling 101
Discussion 108

8 SUMMARY 114
BIBLIOGRAPHY 119

LIST OF TABLES

1.1 List of isolated neutron star detections and a sample of upper limits. Numbered sources are detections, and lettered sources are upper limits. 5

1.2 Listing of standard and non-standard neutrino emission processes. . 6

3.1 Summary of X-ray spectral results from previous observations. OF93 used *ROSAT* PSPC data only, while all others used a combined *ROSAT* PSPC and *ASCA* SIS data set. 23

3.2 Summary of X-ray spectral results from combined *ROSAT* and *Chandra* analysis using models from previous work. A single blackbody component is labeled as BB, and a single power-law component is labeled as PO. The hydrogen column density is n_H. The soft blackbody apparent temperature are labeled kT_S and radius R_S. Similarly, the values for the hard blackbody are labeled with kT_H and R_H. The power-law index is Γ, and the power-law normalization is N_Γ. The fit statistic is χ^2, the degrees of freedom is d.o.f., and $\chi^2_\nu = \chi^2/\text{d.o.f.}$. . . 33

3.3 Summary of X-ray spectral results from combined *ROSAT* and *Chandra* analysis using 3 component model. 36

3.4 Summary of X-ray spectral results from phase resolved *Chandra* analysis using 3 component model, case 1. The fixed parameters are n_H=1.3 $\times 10^{20} cm^{-2}$, R_s=11.6 km at 1 kpc, kT_H=0.14 keV , and Γ=1.66. . . 42

3.5 Summary of X-ray spectral results from phase resolved *Chandra* analysis using 3 component model, case 2. The fixed parameters are n_H=1.3 $\times 10^{20} cm^{-2}$, kT_s=72 eV, R_H=0.82 km at 1 kpc , and Γ=1.66. 42

4.1 Single power-law fit for both observations. The values in the parenthesis are best fit values using the fixed $n_{H,22}$ value from the combined fit. 64

4.2 Blackbody plus power-law fit for both observations. As before, the values in the parenthesis are for the best fit values using the fixed value for $n_{H,22}$ 67

4.3 Phase resolved spectral results for power-law model with $n_{H,22}$ fixed at the phase integrated value of 2.85. 67

LIST OF FIGURES

1.1 Standard cooling curve including the current detections (numbers) and upper limits (letters). See table 1.1 for description of the data. The standard cooling curve is for a $1.4M_{\odot}$ neutron star with an FP EOS and a T72 superfluid model. 4

2.1 *Chandra* CC mode image of 1E1207.4-5209 without correction for spacecraft dither and SIM motion. The image is a negative linear grey scale. The horizontal scale is position at 0.″5 per pixel, and the vertical is time at 2.8 ms per pixel. 16

2.2 *Chandra* CC mode image of 1E1207.4-5209 with correction for spacecraft dither and SIM motion. 17

3.1 One dimensional continuous clocking (CC) mode image of PSR B1055-52. 27

3.2 Z_1^2 (Rayleigh) statistic as a function of frequency for the *Chandra* data set near the radio ephemeris. 29

3.3 Energy resolved light curves of the *Chandra* observation. 30

3.4 Pulsed fraction as a function of energy for the *Chandra* observation . 32

3.5 Results from PSR B1055-52 combined *ROSAT* and *Chandra* analysis using a two component model, two blackbodies. Notice the deviation of high energy photons in the residual. 34

3.6 PSR B1055-52 combined *ROSAT* and *Chandra* analysis using 2 component, blackbody plus power-law with fixed index, Γ=1.5. The distinctive sinusoidal distribution of the residuals indicate a poor fit. . . 35

3.7 Results from our PSR B1055-52 combined *ROSAT* PSPC and *Chandra* ACIS-S3 analysis using three component, two blackbodies plus power-law, model. The top panel shows the raw *ROSAT* (low energy) and *Chandra* (high energy) data sets. The middle panel shows the residual for the fit. The lower panel shows the unfolded spectra with telescope response taken into account. The 3 curves are the soft blackbody component (long dash), the hard blackbody component (dash), and the power-law component (dot). The sum of the three components is the solid line. 38

3.8 Confidence contours for soft blackbody for phase integrated spectrum. The contours are for $n_{H,20}$ versus kT_S and R_S versus kT_S, where $n_{H,20}$ = n_H /10^{20} cm^{-2} and R_S is the soft blackbody radius in km at 1 kpc. The contours are 1 (inner), 1.6 (middle) and 2.6 σ (outer) using a 3 parameter fit. 39

3.9 Confidence contours for the hard blackbody and power-law normalization for the phase integrated spectrum. The contours are for N_Γ versus kT_H and R_H versus kT_H. Again, the contours are using a 3 parameter fit. 40

3.10 Phase resolved spectroscopy results case 1. The fixed parameters are labeled within the panels. The hydrogen column density, n_H was fixed at a value of 1.3 $\times 10^{20} cm^{-2}$. 43

3.11 Phase resolved spectroscopy results case 2. Again, the hydrogen column density, n_H was fixed at a value of 1.3 $\times 10^{20} cm^{-2}$. 44

3.12 Phase variation of blackbody bolometric fluxes (Case I). For the blackbody components the flux was computed by fixing the other parameters to their best fit values for each phase. The errors in the flux were estimated from a χ^2_{min} + 1 contour for the model component. The cgs units are ergs s^{-2} cm^{-2}. 46

3.13 Phase variation of blackbody bolometric fluxes (Case II). See caption for figure 3.12 for details. 47

4.1 Comparison between first (top panel) and second (bottom panel) observation's Z_1^2 statistic. Both are compared to the best fit frequency for observation 1, $f_{0,1} = 0.1933143^{+1.0e-06}_{-1.3e-06}$ Hz. Note the slight shift for the second observation. 57

4.2 Light curve for the first *Chandra* observation. 58

4.3 Light curve for the second *Chandra* observation. 59

4.4 Energy resolved light curves for the first *Chandra* observation. There are insufficient counts below 1 keV and above 8 keV. 60

4.5 Energy resolved light curves for the second *Chandra* observation. The reduction of the observation time leads to an increase of uncertainty. 61

4.6 Energy resolved pulsed fraction for both of the *Chandra* observations. Notice the significant change in the 4-5 keV range. 63

4.7 Combined fit of both *Chandra* observations with a single power-law model. 65

4.8 Combined fit of both *Chandra* observations with a blackbody plus power-law model. 66

5.1 The spectrum of 1E1207.4-5209 *Chandra* data shows the absorption feature which prevented fitting. There is a large deviation in the residual in the range 1.2-1.5 keV. 76

5.2 Fit of absorption edge model for 1E1207.4-5209. The last data point shows the beginning of the background dominated region, but was ignored for fitting purposes. The edge can be seen in the top panel where the best fit line steps down. 78

5.3 Phase resolved spectral fits for 1E1207.4-5209 . The cgs units of flux is erg $s^{-1}cm^{-2}$. The blackbody radius assumes a distance of 15 kpc. 80

7.1 Neutrino emissivity for neutron superfluidity of types A, B, and C. The superfluid critical temperature is chosen to be $T_n^{cr} = 10^9$ K, and the Cooper pair emission mechanism is shut down beyond T_n^{cr} because of no superfluidity above the critical temperature. 95

7.2 Comparison between modified URCA and type B superfluid with superfluid critical temperature of $T_n^{cr} = 10^9$ K. 96

7.3 Comparison between several example superfluid models. For reference nuclear density is 2.8×10^{14} (g cm^{-3}). The models with solid lines are for pions, while all others are neutron $^3P_2$ superfluids. 98

7.4 Standard cooling is shown for a $1.4M_\odot$, FP EOS star with a T72 superfluid. The solid line is the standard cooling curve. The dashed line is the standard cooling including the Cooper pair neutrino emissivity. See figure 1.1 and table 1.1 for summary of data points. 101

7.5 Standard cooling is shown for a $1.4M_\odot$ star with a PS EOS and a T72 superfluid. The solid line is the standard cooling curve. The dashed line is the standard cooling including the Cooper pair neutrino emissivity. See figure 1.1 and table 1.1 for summary of data points. . 102

7.6 Pion cooling with E1 superfluid model a $1.4M_\odot$ star with for the FP EOS. The dotted curve is for standard cooling for a star with $1.4M_\odot$ FP EOS and a T72 superfluid model without Cooper pair emission. The dashed curve is the E1 superfluid suppression for pion cooling with the LM factor $\tilde{g}' = 0.6$ without the Cooper pair effect. The solid curve includes the effect of Cooper pair neutrino emission on pion cooling. See figure 1.1 and table 1.1 for summary of data points. 107

7.7 Pion cooling with the modified E1 superfluid model a star with the pion FP EOS and $1.4M_\odot$. The heavy solid curve is for standard cooling with a T72 superfluid and $1.2M_\odot$, including Cooper pair emission. The other curves are for nonstandard (pion) cooling with the LM, $\tilde{g}' = 0.6$. Each curve represents a different value of ΔT: dotted (ΔT=0), long dashed (ΔT=0.2), chain (ΔT=0.4), dashed (ΔT=0.6), and solid (ΔT=0.8). 109

7.8 Interior temperatures of non-standard and standard cooling as a function of internal density. The labels are the age in log (years). See text for explanation. 110

7.9 Comparisons between equations of state. The critical density for pions, ρ_{crit}, establishes the correct equation of state for neutron stars with masses near $1.4M_{\odot}$. EOSs become unstable when their masses begin to decrease with increasing density. 112

ABSTRACT

New and exciting results for measuring neutron star surface temperatures began with the successful launch of the *Chandra* X-ray observatory. Among these results are new detections of neutron star surface temperatures which have made it possible to seriously test neutron star thermal evolution theories. The important new temperature determination of the Vela pulsar (Pavlov, et al., 2001a) requires a non-standard cooling scenario to explain it.

Apart from this result, we have measured PSR B1055-52's surface temperature in this thesis, determining that it can be explained by standard cooling with heating. Our spectral fit of the combined data from *ROSAT* and *Chandra* have shown that a three component model, two thermal blackbodies and an non-thermal power-law, is required to explain the data. Furthermore, our phase resolved spectroscopy has begun to shed light on the geometry of the hot spot on PSR B1055-52's surface as well as the structure of the magnetospheric radiation. Also, there is strong evidence for a thermal distribution over its surface. Most importantly, the fact that PSR B1055-52 does not have a hydrogen atmosphere has been firmly established.

To reconcile these two key observations, on the Vela pulsar and PSR B1055-52, we tested neutron star cooling with neutrino processes including the Cooper pair neutrino emission process. Overall, it has been found that a phase change associated with pions being present in the cores of more massive neutron stars explains all current of the data. A transition from neutron matter to pion condensates in the central stellar core explains the difference between standard and non-standard cooling scenarios, because the superfluid suppression of pion cooling will reduce the emissivity of the pion direct URCA process substantially. A neutron star with a mass of $1.2M_{\odot}$ with a medium stiffness equation of state and a T72 type neutron superfluid models the standard cooling case well. A neutron star of $1.4M_{\odot}$, with a pion core, with the same type of equation of state modified for pion matter and a modified E1-0.6 pion superfluid model is the best option for the non-standard case. The results also suggest that the equation of state for neutron stars may have to be stiffer than medium.

Furthermore, our observational results from two other sources, SGR 1900+14 and 1E1207.4-5209, have helped us to expand the understanding of isolated neutron stars. The *Chandra* observation of SGR 1900+14 has strengthened the case that it is a magnetar, as the pulsed fraction and the spectral fits suggest a blackbody plus power-law model is prefered. Also, our analysis of the *Chandra* data of 1E1207.4-5209 suggests that it should have a hydrogen atmosphere. Future observations will certainly give even better insight to both of these objects, as well as PSR B1055-52.

CHAPTER 1

INTRODUCTION

The ability of measuring an isolated neutron star surface temperature has become a much easier task in recent years, because of the improvements in the orbiting observatories. The original *EINSTEIN* observatory, launched in 1978, gave the first indication of neutron star surface temperatures. It established upper temperature limits for many neutron stars, and created the first hope of beginning to reconcile theory with observation (e.g. Nomoto & Tsuruta 1981, 1986). Later, with the launch of *ROSAT*, the Röntgen Satellite developed mainly by Germany, the United States and the United Kingdom which was launched in 1990, three convincing detections were made for pulsars PSR B0656+14, PSR B1055-52, and Geminga. Afterwards, a few more neutron star's surface temperature measurements followed with the launch of *ASCA*, the fourth Japanese X-ray astronomy mission launched in 1993, and ground based optical telescopes. Finally, the introduction of *Chandra*, detailed in chapter 2, and *XMM-Newton*, the European Space agency's X-ray multi-mirror satellite, have improved the detection capabilities beyond all previous levels.

Neutron stars are thought to be born in supernova explosions. They are what

remains of the core of the progenitor star. If the core is above a certain mass, which remains uncertain but is estimated to be $\sim$2-3$M_{\odot}$, the core will collapse into a black hole; otherwise, a neutron star is formed. The neutron star will begin life at extremely high temperatures, with core temperatures as high as $\sim 10^{10-11}$ K, and cool off by various mechanisms.

The importance of detecting a neutron star's surface temperature relates to their thermal evolution. A neutron star first cools via various neutrino emission mechanisms, from the interior of the star, before the photon radiation from the surface becomes the dominant cooling process (Tsuruta, 1979). The first thermal evolution calculations (Tsuruta, 1964) showed that a neutron star should be visible as an X-ray source for about a million years. Among the important factors which seriously affect the nature of thermal evolution are the neutrino emission processes, the superfluidity of the core particles, the composition, and the mass of the neutron star.

The conventional neutrino cooling mechanisms, adopted in the earlier and most of the subsequent cooling calculations, such as the modified URCA, plasmon neutrino and bremsstrahlung processes, are called 'standard' cooling. On the other hand, the more exotic and extremely fast cooling processes, such as the URCA process involving pions, kaons, and quarks, and the direct URCA process involving nucleons and hyperons, are called 'nonstandard' processes (Tsuruta, 1998).

Once all neutrino cooling rates have decreased below the surface photon cooling rate, the photon cooling from the surface of the star takes over, dictating the remainder of the thermal evolution. Even though at earlier times the neutrino mechanisms

control the thermal evolution, the neutron star will emit photons from its surface. Consequently, through much of their earlier thermal history, neutron stars should remain visible as X-ray sources.

Measuring an isolated neutron star's temperature becomes important to test various thermal evolution theories. If a neutron star cools slowly through the standard cooling, its surface temperature will be higher than if it cools rapidly through non-standard cooling. Overall, early upper limits and detections showed that the standard cooling process would explain all the data, except for the Vela pulsar's upper limit. Later, as more observed temperatures became available, possible exceptions to standard cooling began to be discussed. Although, thermal evolution has been primarily a theoretical problem for many years, dating back to the nineteen-sixties (Tsuruta, 1964). It has only recently become a serious observational problem, with the addition of many more detections.

Figure 1.1 shows a typical standard cooling curve along with upper limits and detections of various isolated neutron stars. The upper limits shown here are mostly from *ROSAT* and combined *ROSAT* and *ASCA* observations. For RCW 103, both the upper limit based upon earlier *EINSTEIN* observation (c) and the new upper limit based upon new results (c*) using *XMM-Newton* (Slane, 2001) are shown. In addition to the original three detections, PSR B1055-52 (6), PSR B0656+14 (4), and Geminga (5), additional new detections have been established. The new point, Vela (3) from the *Chandra* observation, together with the new RCW 103 upper limit (c*) are the most important addition to the detection list, as its surface temperature

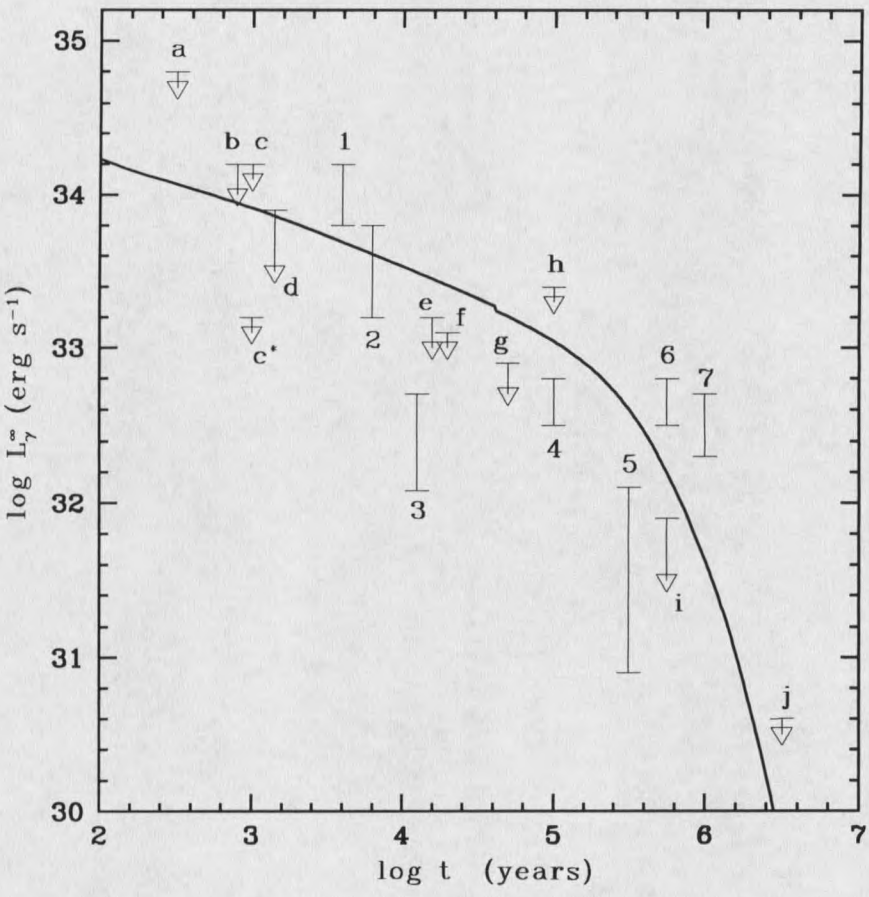

Figure 1.1: Standard cooling curve including the current detections (numbers) and upper limits (letters). See table 1.1 for description of the data. The standard cooling curve is for a $1.4M_\odot$ neutron star with an FP EOS and a T72 superfluid model.

makes it an important candidate for non-standard cooling. The point source in Cas A (a), is included as an upper limit, even though the case for Cas A being a neutron star is far from certain (e.g. Pavlov et al, 2000, Umeda et al, 2000). Table 1.1 gives a summary of all the detections and upper limits.

The cooling curves are made using our 'exact' evolutionary code, where no isothermal approximation is made. This differs from isothermal codes because it includes the finite time scale of thermal conduction through the neutron star crust. The conduc-

Table 1.1: List of isolated neutron star detections and a sample of upper limits. Numbered sources are detections, and lettered sources are upper limits.

Source	Name	Reference
1	RX J0822-43	Zavlin, Trümper, & Pavlov, 1999
2	1E1207.4-5209	Zavlin, Pavlov & Trümper, 1998
3	Vela	Pavlov et al., 2001a
4	PSR B0656+14	Becker, 1995
5	Geminga	Becker, 1995
6	PSR B1055-52	Ögelman & Finley, 1993
7	PSR RX J185635-3754	Walter, Wolk, & Neuhäuser, 1996
a	Cas A point source	Pavlov et al., 2000
b	Crab pulsar	Becker, 1995
c	RCW 103	Tuohy & Garmire, 1980
c*	RCW 103	Slane, 2001
d	PSR B1509-58	Becker, 1995
e	PSR B1706-44	Becker, 1995
f	PSR B1823-13	Finley, Srinivasan, & Park, 1993
g	PSR B2234+61	Becker, 1995
h	PSR B1951+32	Becker, 1995
i	PSR B0355+54	Becker, 1995
j	PSR B1929+10	Becker, 1995

tion time scale depends upon the neutron star model of the equation of state (EOS) detailing the pressures associated with the strong nuclear force. For the softest EOS, BPS (Baym, Pethick & Sutherland, 1971), the conduction time scale is $\sim$100 years. For the FP (Friedman and Pandharipande, 1981) EOS, which is of medium stiffness, it is $\sim$1000 years. For the PS (Pandharipande, Pines & Smith, 1976) EOS, for stiff matter, it is up to $\sim 10^4$ years. The cooling curves for the exact and the isothermal codes converge after those times. At present various neutron star EOSs are available (e.g. Wiringa, Fiks, & Fabrocini, 1988, and Nishizaki, Takatsuka, & Hiura, 1994), but we chose BPS, FP, and PS as representative EOSs for comparison to previous

results (e.g. Tsuruta, 1998).

Table 1.2 gives a listing of the standard and non-standard neutrino processes. The standard cooling is dominated by the modified URCA neutrino process (Friman

Table 1.2: Listing of standard and non-standard neutrino emission processes.

Standard	Non-standard
Modified URCA	Direct URCA (nucleons)
n-n bremsstrahlung	Pion URCA
n-p bremsstrahlung	Kaon URCA
plasmon neutrino	Hyperon URCA
Nuclear URCA	Quark URCA
e^--heavy ion bremsstrahlung	
e^--e^+ pair neutrino	
photo-neutrino	

and Maxwell, 1979, FM79 hereafter). The other processes are the neutron-neutron neutrino bremsstrahlung, neutron-proton neutrino bremsstrahlung (FM79), nuclear URCA (Tsuruta and Cameron, 1965), the electron-heavy ion neutrino bremsstrahlung (Itoh and Kohyama, 1984), and the plasmon neutrino, photo-neutrino, and electron-positron pair neutrino processes (Munakata et al., 1985). Overall, the modified URCA, and the neutron-neutron and neutron-proton neutrino bremsstrahlung processes in the central core produce the highest neutrino emissivity, though all of the standard cooling processes are accounted for in the cooling code used for this work. However, during the earliest stage of cooling when the information on the cooling in the central core has yet to be transmitted to the surface due to the finite time scale of thermal conduction, the surface cools due to the plasmon neutrino, the nuclear

URCA, and the electron-heavy ion bremsstrahlung processes operating in the inner crust.

The non-standard cooling has many options depending upon the composition of the core of a neutron star. By assuming the core is entirely nucleons with sufficiently high proton concentration, the validity of the direct URCA process for nucleons is pointed out (Lattimer et al., 1991). If the core is composed of pions, then the pion direct URCA process can take place (Muto, et al. 1988). Similarly, if kaons or quark matter is present, then corresponding kaon or quark direct URCA process is possible (Tatsumi, 1988 and Iwamoto, 1980).

To match the new observations, the choice of non-standard cooling has to be made; however, all of the non-standard cooling scenarios cool entirely too fast to be considered without some sort of suppression of their rates (e.g. Tsuruta, 1998). Fortunately, the core of neutron stars are expected to be in a superfluid state. Unlike terrestrial superfluids, under the ultra-high densities present in neutron star cores that are higher than the density of an atomic nucleus, the temperature is relatively high when core particles become superfluid. Typical superfluid critical temperatures, T_{cr}, below which superfluidity sets in, occurs in some cases at $T_{cr} \sim 10^8$ K. Superfluid suppression of a non-standard neutrino emission mechanism slows the cooling rate such that non-standard cooling curves can approach the standard cooling curves. Some superfluid models have a very high T_{cr}, which essentially shuts down all the non-standard cooling process. Other superfluid models have T_{cr}s that are too low, which fail to suppress the non-standard cooling sufficiently to explain the data. The

challenge is to choose a superfluid model that has the right amount of suppression. Page (1990) began this exploration, showing cooling using various gap energies, and other authors have followed with improved physical models (e.g. Umeda, Tsuruta, & Nomoto, 1994, and Page, 1998).

From the observational standpoint, measurement of the relevant parameters has been improved with the newer generation of X-ray telescopes. First off, the distance to these objects has been difficult to measure. Using the fits for the observational data, there is a ratio of distance with some other parameter, which in turn is unknown. For example, a blackbody radiator model gives a normalization that is given by $(R_S/d)^2$, where R_S is the apparent effective radius at distance d. The apparent effective radius R_S relates to the real radius R by $R_S = e^{-\phi_s/c^2}R$, where $e^{\phi_s/c^2} = (1 - 2GM/Rc^2)^{1/2}$ is the surface red-shift factor, with M being the gravitational mass and G the gravitational constant. Often, the distance to the neutron star is inferred from assuming that the effective radius is $\sim$10 km. Other methods of estimating the distance are also used to verify this assumption, but lacking a direct distance measurement will not constrain the radius. However, the availability of multi-wavelength observations and improved spectral resolution of X-ray telescopes have helped constrain the normalization by giving better distances and lowering the uncertainty.

Furthermore, getting the temperature has been improved. Often there are local areas of increased temperature, hot-spots (e.g. Greiveldinger, et al., 1996), which makes the model fitting more difficult since both the hot-spot and the stellar surface

have to be simultaneously fitted. With a sufficiently high number of measured X-ray photons, separating the two components has became increasingly easier with improved spectral resolution. Additionally, the magnetic fields associated with many neutron stars are thought to be very high, $\sim 10^{12}$ Gauss for a typical pulsar. In such a high field, a magnetospheric pair plasma is thought to exist (e.g. Wang, et al., 1998). The non-thermal process involving this plasma does emit X-rays, so they also have to be considered when attempting to fit the data. Beyond this, there are also potential physical effects of the environment which might distort the direct measurement of the surface temperature; however, improved spatial resolution has helped to minimize this. The most notable is the effect of the interstellar medium. Neutral hydrogen absorbs radiation very efficiently in the ultraviolet range of energies, and this effect extends into the X-rays. Fitting the data requires including the effect of interstellar absorption, which can be constrained by multi-frequency observations.

Additionally, the neutron star's surface can modify the emitted radiation from a pure blackbody radiator. One of the most pronounced effects is that of an atmosphere (e.g. Romani, 1987). Fits of hydrogen atmosphere models have shown effective temperatures for several neutron stars that are lower than blackbodies (e.g. Pavlov et al., 1994). The most dramatic example of hydrogen atmosphere models is for the Vela pulsar, which has shown that its surface temperature is much lower and a radius that is much larger than what a blackbody model would predict (Pavlov et al., 2001a). Consequently, improvements in atmosphere models have made getting the effective temperature a much easier task.

If getting all of this information is difficult with just the X-ray spectrum, observational information from other wavelengths provides the clues to many of the challenges. For example, looking at the γ-ray energies will give clues about the magnetospheric radiation; furthermore, an optical and/or UV observation can also constrain the temperature as well as the magnetospheric radiation. Many of the isolated neutron stars also happen to be radio pulsars. Getting constraints on the rotation angles and magnetic axes from the radio observations give clearer pictures to the model that should fit the X-ray data. Periodic variation of X-rays from a pulsar allows timing analysis and production of light curves. *RXTE*, the Rossi X-ray timing explorer, which covers a higher X-ray energy band than does either *ROSAT* or *ASCA*, provides good timing information for brighter sources, as do *Chandra*'s capabilities. *Chandra* also provides the ability to begin the analysis of phase resolved spectroscopy which in turn should begin to put tighter constraints on the physical models.

In addition, observation has driven new theoretical considerations. The discovery of magnetars, isolated neutron stars with huge, $\sim> 10^{14}$ Gauss magnetic fields, led to drastic modification to thermal evolution theories, since magnetar surface temperatures were far in excess of temperatures predicted by standard cooling of non-magnetized neutron stars. Several authors (e.g. Heyl and Hernquist, 1997) have done extensive work on the cooling of a magnetar. Though magnetar thermal evolution is an important theoretical consideration, it is beyond the scope of the cooling theory presented herein.

For the thermal evolution theory of isolated neutron stars, observation will estab-

lish the extents for the neutron star surface temperatures. The theoretical challenge will be establishing thermal evolution theory which explains all of the data in a concise physically reasonable way.

The scope of our work includes both the observational and theoretical challenges in part. Our work to measure neutron star surface temperature using one of the newest tools, the *Chandra* X-ray observatory, will be presented in chapters 3-5, while chapter 2 introduces *Chandra* and chapter 6 discusses briefly the future of neutron star observations. The *Chandra* observation of PSR B1055-52, in chapter 3, shows that the surface temperature remains about the same as previous *ROSAT* and *ASCA* results, but we found a three component model to be the best fit to the data, contrary to their two component models. In chapter 4, we show our results of the *Chandra* data analysis of SGR 1900+14 immediately following its most recent outburst, indicating that the magnetar model is a good explanation for the results. Chapter 5 shows our new spectral results of the *Chandra* data analysis of 1E1207.4-5209, indicating that a hydrogen atmosphere is required. Chapter 7 presents our results for the theoretical challenge offered by the new observations, with the effects of Cooper pair neutrino emissivity. We show that the correct choice of superfluid with pion cooling can explain all the currently available data. A summary, in chapter 8, will give the key observational and theoretical results.

CHAPTER 2

CHANDRA X-RAY OBSERVATORY

Introduction

The *Chandra* X-ray Observatory (CXO) was formerly known as AXAF, the Advanced X-ray Astrophysics Facility. Its capabilities were intended as a combination of the *ROSAT* and *ASCA* energy range with improved spatial and spectral resolution, with a larger effective area. The spatial resolution was accomplished by the combination of the high resolution mirror assembly (HRMA) combined with the small pixel size of the Advanced CCD Imaging Spectrometer (ACIS) and with the High Resolution Camera (HRC) chips. Spectral information is complemented by two gratings, the Low Energy Transmission Grating (LETG) and the *Chandra* High Energy Transmission Grating (HETG).

The HRMA is a set of four paraboloid-hyperboloid (Wolter-1) nested pairs that are 1.2 meters in diameter. The mirrors are grazing-incidence so that the X-rays do not penetrate deep into the mirror material before being reflected. The mirrors are coated with iridium to a depth of 30 nm. The effective area of the mirrors runs from

$\sim$800 cm^2 at 0.5 keV and drops down to $\sim$400 cm^2 at 2.0 keV, then steadily drops off at higher energies. The large effective area of the mirror make the spatial and spectral resolution the best yet made.

At the rear of the telescope in the focal plane is the Scientific Instrument Module (SIM). The SIM contains the ACIS and HRC chips along with the LETG and HETG gratings. The various instruments can be brought into focus and can be used for observations depending upon the scientific objectives.

The ACIS is an array of 10 CCDs. Four of the CCDs are designed especially for imaging, being designated the ACIS-I. They are arranged in a square, 2 x 2 array, at the center of the focal plane. Below the ACIS-I on the focal plane, are the 6 ACIS-S CCDs, designed for spectral work in imaging mode or with one of the two gratings. Two of the CCDs are back illuminated, while the other 8 are front illuminated. The ACIS CCDs have excellent spatial resolution, $\sim$0.″5 full width half maximum (fwhm). The timing resolution is $\sim$3 s in imaging mode; however, the ACIS-S3 can be used in Continuous Clocking (CC) mode, improving the timing resolution to $\sim$3 ms, but the image is reduced to 1 dimension.

The HETG is the principle grating to be used with the ACIS-S CCD array. The grating is composed of two gratings for high and medium energies, the High Energy Grating (HEG) and the Medium Energy Grating (MEG). The HEG and MEG are offset from each other on the ACIS array to avoid overlap so that the spectral information can be used simultaneously.

The HRC consists of a set of two Micro-Channel Plate (MCP) type detectors. One

is optimized for imaging (HRC-I) and the other is a readout for the LETG (HRC-S). The HRC-I has the largest field of view of all of *Chandra* instruments giving a half degree by half degree image. The spatial resolution of the HRC detectors are $\sim 0\farcs4$ fwhm. The spectral range for the HRC is larger than that of the ACIS, but the spectral resolution is much less for the HRC-I. The timing resolution of the HRC is the best available on *Chandra* , having 16 μs resolution.

The LETG is the grating for the HRC-S detector, though it can be used with the ACIS-S array. The energy range with the HRC-S is 70-7290 eV and 200-8860 eV with the ACIS-S. The resolution for a spectral line in these ranges is $\sim$ 0.005 nm fwhm, having the highest resolving power available on *Chandra* at low energies (0.08-0.2keV). The LETG in combination with the HRC-S allows time resolved spectra and spatially resolved spectra of multiple sources (*Chandra* Proposers Observatory Guide, 2000).

Data Reduction

The data reduction for *Chandra* is an involved process for each of the different instruments and modes available. Since our work primarily involves the use of the ACIS-S3 chip in CC mode without any gratings, the discussion will be confined to procedures for that chip and mode. Similar procedures can be used for the ACIS in imaging mode. The analysis is performed using utilities from the *Chandra Interactive Analysis of Observations* (CIAO) software package, available from the *Chandra X-*

ray Center (CXC), and the xspec spectral analysis program, available from the High Energy Astrophysics Science Archive Research Center (HEASARC).

The raw data received by the CXC at Harvard University, is first run through some pre-processing, called pipeline processing, before being made available to the individual observers. This procedure sets up the data in a usable form for the user. The raw data, without any pipeline processing, is available, but its use is not recommended. Bias correction, overclock correction and coordinate transformations are applied to the data in this process. Also, any events which are certain to be considered bad due to background flares or solar activity are removed. Once the processing pipeline has been produced, the data is made available to the users (Data Products Guide, 2001).

The first important procedure that we must perform is to correct the observation for spacecraft dither and SIM motion. This affects the position and the time of the event, because the y-axes of the chip is used to compute time. Figure 2.1 shows the raw event file prior to the correction. Without the correction, the timing analysis is flawed, producing several periods near the actual period, and spectral analysis has a potential for flaws, because of the increased background. Correcting for this motion requires applying the following correction:

$$t_{corr} = t + t_o \; sin\xi \; (\alpha - \alpha_{med}) \; cos\delta_{med} - t_o \; cos\xi \; (\delta - \delta_{med}), \qquad (2.1)$$